JMEPEG (2012) 21:1813–1823
DOI: 10.1007/s11665-011-0068-0

1059-9495/$19.00

Spall-Fracture Physics and Spallation-Resistance-Based Material Selection

M. Grujicic, B. Pandurangan, B.A. Cheeseman, and C.-F. Yen

(Submitted July 29, 2011)

Spallation is a fracture mode commonly observed in ballistically/blast-wave-loaded structures. The interaction between decompression waves generated within the target structure produces tensile stresses which, if of a sufficient magnitude, may cause material damage and ultimate fracture (spallation). In this study, the phenomenon of spall-fracture is analyzed within a one-dimensional Lagrangian framework. Two distinct analyses are carried out. Within the first analysis, decompression waves are treated as decompression shocks, which simplified the analysis and enabled the formation of spallation-strength-based material index. In the second analysis, decompression waves are treated as smooth (centered simple) waves. This increased the fidelity of the computational analysis, but the material-selection procedure could be done only numerically and an explicit formulation of the spallation-strength-based material-selection index could not be carried out. Overall, the two analyses yielded similar results for the spallation-strength-based material-selection criterion suggesting that the simpler (decompression shock based) one is still adequate for use in the material-selection process.

Keywords material-selection methodology, spall-fracture, spallation resistance

1. Introduction

This article deals with *spall-fracture* or *spallation*, an important scientific and technological phenomenon. Spallation is a fracture mode generally observed in ballistically (i.e., projectile impacted) and/or blast-loaded target structures in which loading is applied dynamically through the generation, propagation, and interaction of various compression/recompression shocks and decompression waves. As will be shown below, the interactions of these shocks and waves produce material states within the target which are associated with tensile stresses. When these stresses are of a sufficient magnitude and persist over a sufficiently long time period, formation of a diffuse distribution of microcracks or voids in the interior of the target may take place. Complete fracture then may result from coalescence of individual microcracks and voids. This produces a sheet-like fragment at the back of the target which is propelled in the projectile/blast-wave initial propagation direction. This description of the spall-fracture process indicates that when designing ballistic/blast protective structures, it is not sufficient to only ensure that these structures are not defeated/penetrated but also that no-spallation takes place. In Fig. 1, an example of spallation-induced damage investigated in our recent work (Ref 1) is displayed.

M. Grujicic and **B. Pandurangan**, Department of Mechanical Engineering, Clemson University, 241 Engineering Innovation Building, Clemson, SC 29634-0921; and **B.A. Cheeseman** and **C.-F. Yen**, Army Research Laboratory—Survivability Materials Branch, Aberdeen, Proving Ground, MD 21005-5069. Contact e-mail: gmica@clemson.edu.

The dominant form of the spallation-induced damage depends on the intrinsic ductility of the target material. For example, in brittle materials spallation typically produces microcracks with crack faces parallel with the target back face. In sharp contrast, typical spallation-induced damage in ductile materials is in the form of rounded voids. The aforementioned distinct nature of the spallation-induced damage in these two classes of materials is generally present only at lower damage levels. At larger damage levels, this distinction is often less apparent as in brittle materials the cracks tend to acquire larger openings, while in ductile materials voids become elongated and their coalescence leads to the formation of crack-like flaws. In addition, in materials of intermediate ductility the damage morphology may contain both crack- and void-like features (Ref 2).

Traditionally, the onset of spallation is analyzed within the context of the so-called spall criterion, a mathematical condition involving stress, strain, temperature, and other continuum field variables which must be satisfied for spallation to occur. In this case, spall-fracture is considered to be a discrete/binary event; either it has taken place or not (Ref 2). Frequently, the spall criterion is supplemented with the concept of an incubation period, i.e., a minimum time period over which the spall criterion must be satisfied for the spall-fracture to occur.

In recent years, spallation-induced damage and ultimate spallation fracture are considered as evolving processes. This was done to comply with experimental observations that clearly showed that damage develops gradually by a process of nucleation, growth, and coalescence of micro-flaws (microcracks and/or microvoids) (Ref 3). Recently, continuum theories have been proposed to explain the process of spallation-induced damage evolution observed in ballistically/blast-wave-loaded target structures (Ref 4). Such theories take into account the effects of the evolving damage on the residual stiffness/strength of the target material and, thus, on the spatial

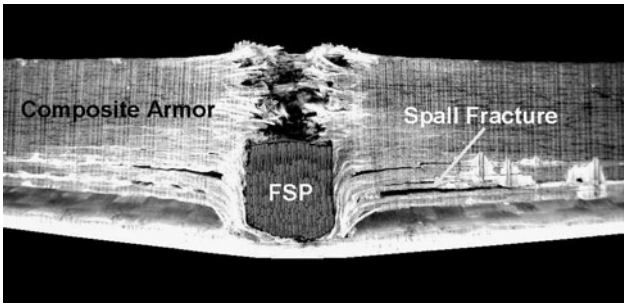

Fig. 1 Experimentally determined material damage distribution resulting from the impact of a 0.50 caliber right circular cylinder (RCC) solid-steel fragment simulating projectile (FSP) with a 25.4 mm thick (53 vol.%) E-glass continuous-fiber reinforced polyvinyl-ester-epoxy matrix composite armor. Initial projectile velocity: 605 m/s (Ref 1)

distribution and temporal evolution of stress (and other continuum field variables) which governs the spall-fracture process. In these theories, the spall criterion has been replaced with the criterion for the onset of spallation-induced damage, with one or more damage-evolution and material-property degradation equations and with a condition at which complete spall-fracture occurs (Ref 5–8).

Post-mortem microscopic observations of ballistically/blast-loaded structures often reveal the site of damage initiation and details of the subsequent damage-evolution process(s). Detailed analysis of this experimental information could be highly beneficial in elucidating the intrinsic spall-fracture resistance of the material at hand. This knowledge, in turn, can guide the selection of the materials for use in protective structures.

While practical solutions of the real-world spall-fracture problems entail the use of more elaborate computer-aided engineering and transient non-linear dynamics computational analyses, a good insight into the spallation-fracture phenomenon can be gained by analyzing this phenomenon under simplified one-dimensional conditions. These conditions are encountered in the so-called flyer-plate experiments (reviewed in section 2). As will be shown in the subsequent sections, planar compression/recompression shocks and decompression shocks/waves are generated, propagated, and interacted within the target structure in the case of flyer-plate impact experiments. It will also be shown that as a result of the interaction of two sufficiently strong planar decompression waves (sometimes approximated as decompression shocks), regions within the target become subjected to high enough tensile stresses so that spallation-induced damage and fracture may occur. Depending on the strength of the decompression waves, spallation-induced damage of various degrees (from few isolated cracks to complete fracture and separation/detachment of a layer of material) can take place within the target material.

It should be noted that a clear distinction is made in this article between (planar) shock waves (or shocks) and (planar) smooth waves. Shocks are waves with a vertical wave front which produces an abrupt/discontinuous change in the material state variables upon passage through a material point. The discontinuous change (also known as a "jump") in the material states produced by a shock is governed by a set of so-called shock-jump equations. The locus of all-possible (shock-strength dependent) as-shocked material states from a given material initial state is represented by a hyper-curve known as a Hugoniot curve within a stress/mass-density/energy-density/particle-velocity/… multi-dimensional space. Smooth waves, on the other hand, possess an extended wave front and, hence, cause a gradual change in the material state variables as they pass through a material point. It is well established that smooth-wave induced changes in the material states are often of an isentropic (constant-entropy) nature. In the weak-shock regime, it is generally justified to approximate smooth-wave isentropes with the corresponding shock-Hugoniots. This approximation will be used in this study.

The main objective of this study is to carry out a one-dimensional analysis of the spall-fracture process in the weak-shock regime in which the loading rate is sufficiently high to produce spallation-induced damage but does not induce plasticity. In other words, it is assumed that under high loading-rate conditions analyzed, the material yield strength is increased above the material fracture strength. Spallation within elastic-plastic materials will be analyzed in a future communication. In addition to analyzing the spallation process, an attempt will be made to establish the basic material-selection criteria for use in protective structural applications in which a low probability for spallation may be an important functional requirement.

The organization of this article is as follows: In section 2, a brief description is provided of the flyer-plate experiments which are used to produce, detect, and quantify the extent of spallation-induced damage. In section 3, the spall-fracture phenomenon is analyzed as a result of the intersection of two decompression shocks. In other words, smooth decompression waves are approximated as two discontinuous shocks, in this case. In section 4, interaction of two smooth decompression waves and the associated spallation process are analyzed. A comparison of the results obtained in section 3 and 4 and preliminary development of the spallation-resistance-based material-selection criteria are presented in section 5. A summary of the main findings and conclusions is provided in section 6.

2. Experimental Analysis of the Spall-Fracture Process

In this section, a brief description is provided of the typical experimental set-up/procedure used to produce and detect spall-fracture in materials under investigation. A schematic of this set-up is depicted in Fig. 2. In the experimental arrangement shown in this figure, a plate-shaped projectile impacts a plate-shaped target in such a way that the projectile/target contact is initially established at the same time over the entire projectile/target contact surface. This experimental set-up is often referred to as a "flyer-plate" experiment. Typically the projectile thickness L_p is smaller than the target thickness L_T so that spallation occurs within the target. Also, it is generally convenient to have the projectile and the target made of the same material (the so-called symmetric flyer-plate experiment), since the particle-velocity jump associated with the incident shocks generated at the projectile/target contact surface is equal to one half of the projectile initial velocity. In other words, this particle-velocity jump does not need to be measured separately, making the experimental procedure simpler. As will be shown below, reflection of the two incident shock waves from the projectile and target back surface produces decompression/release waves and it is the intersection of these release waves which is ultimately responsible for spall-fracture.

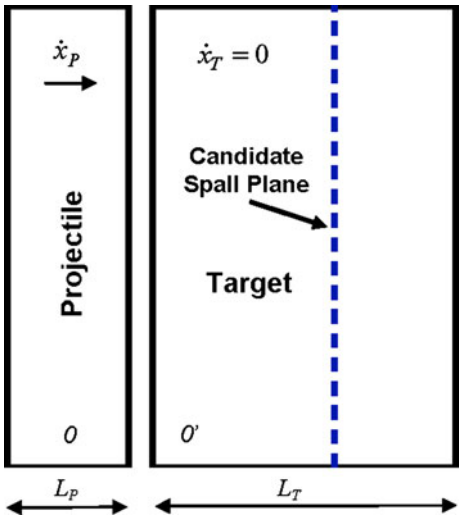

Fig. 2 A schematic of the flyer-plate experimental set-up used in the investigation of spall-fracture phenomenon. It should be noted that for clarity, the projectile and the target thicknesses have been exaggerated relative to their lateral dimensions

As mentioned earlier, numerous experimental investigations have clearly demonstrated that spallation-induced damage develops gradually by nucleation, growth, and coalescence of micro-flaws. It should be noted that, flyer-plate experimental conditions can be selected in such a way that spallation-induced damage-evolution process can be arrested at any stage of its evolution. This can greatly facilitate the investigation and the quantification of this material-degradation process.

3. Spall-Fracture Due to Interaction of Two Decompression Shocks

While practical solutions of the real-world spall-fracture problems entail the use of more elaborate computer-aided engineering and transient non-linear dynamics computational analyses, a good insight into the spallation-fracture phenomenon can be gained by analyzing this phenomenon under simplified one-dimensional conditions (corresponding to the conditions encountered in the aforementioned flyer-plate experiments).

3.1 Simplifying Assumptions

The phenomenon of spall-fracture within a one-dimensional framework is analyzed in this section using a highly simplified (yet fairly realistic) approach. The material analyzed in this section and in the remaining sections is assumed to be a "normal material," i.e., a material which supports the formation of a shock during compressive loading. Within this approach, the following simplifying assumptions are made:

(a) The material mechanical response is assumed to be governed by a single (normal) Hugoniot relation. This relation defines the possible as-shocked material states during compressive loading;
(b) As far as the decompression is concerned, it is assumed to take place by the propagation of "decompression shocks". Thus, the Hugoniot relation defines also the possible (discrete) unloaded states resulting from the propagation of the decompression shocks. In the subsequent sections, however, decompression will be assumed to result from the propagation of smooth (centered simple) decompression waves. In this case, the same Hugoniot relation will be used as an approximation for the associated "decompression isentrope" and employed to derive a continuous set of states present within the decompression waves; and
(c) The projectile and the target are assumed to be made of the same material so that the strength of the two incident shocks (as measured by the jumps in the associated particle velocities) can be directly determined from the knowledge of the projectile initial velocity.

3.2 Material State Evolution Preceding and Following Spall-Fracture

A sequence of events and the resulting material states following the projectile/target initial collision are depicted in Fig. 3(a) to (d). The initial state of the materials residing within the projectile and the target are denoted as 0 and 0′, respectively.

As shown in Fig. 3(a), upon the collision, two diverging shocks are formed each producing a particle-velocity jump equal to $\frac{\dot{x}_P}{2}$, where $\dot{x}_P$is the projectile initial velocity. Consequently, the projectile material swept by the left-propagating shock is decelerated to $\dot{x} = \frac{\dot{x}_P}{2}$, while the target material swept by the right-propagating shock is accelerated to $\dot{x} = \frac{\dot{x}_P}{2}$. The resulting as-shocked material state within the projectile and the target is denoted as 1.

Figure 3(b) shows that upon reflection of the two incident shocks from their respective back face free surfaces, two converging decompression shocks are formed (one at the projectile back face and the other at the target back face). The material states produced by the two decompression shocks are denoted as 2 ($\dot{x} = 0,\ -t_{11} = 0$) and 3 ($\dot{x} = \dot{x}_P,\ -t_{11} = 0$) for the right and left-propagating decompression shocks, respectively. It should be noted that the right-propagating decompression shock passes through the projectile/target contact surface without interaction since the two are composed of the same material and state 2 behind right-propagating shock is associated with a non-tensile axial stress.

After the intersection of the two converging decompression shocks, Fig. 3(c), a new state of the material (denoted as state 4) within the target is produced. As will be shown below, the material in state 4 is subjected to tension and if the tensile stress is sufficiently high, spallation fracture will occur. However, while drawing Fig. 3(c), it is assumed that spallation fracture is preceded by and incubation period so that fracture does not occur at the very instant of intersection of the two converging decompression shocks.

Following a brief incubation period, spallation is assumed to take place at the original intersection plane (often referred to as the "candidate spall plane") of the two converging decompression shocks. In the case of a symmetric flyer-plate impact, analyzed here, the candidate spall plane is located at a distance equal to the projectile thickness from the target back face. Spall-fracture produces two stress-free/unrestrained surfaces and subsequently two diverging "recompression" shocks as seen in Fig. 3(d). The associated zero-stress material states are denoted as 6, behind the left, and 7, behind the right-propagating recompression shock.

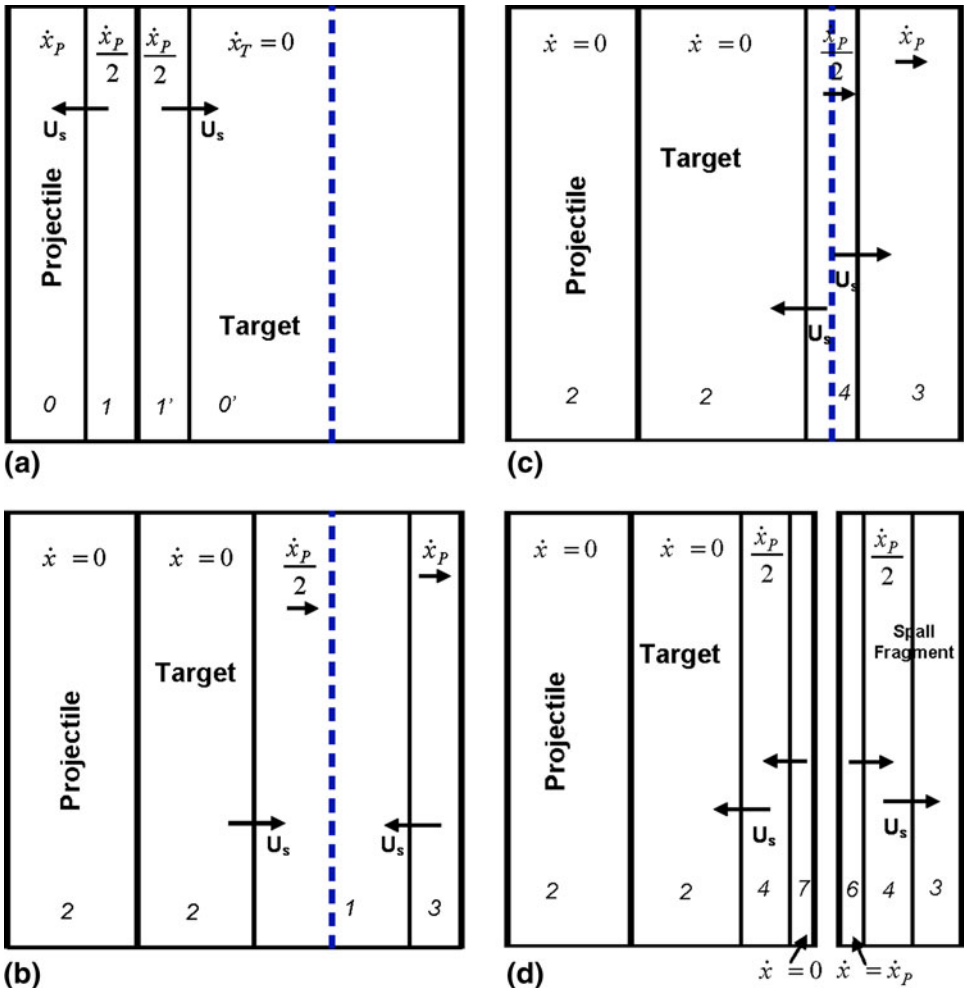

Fig. 3 Compression-shock reflections from the unrestrained surfaces and the decompression-shock interactions in the interior of the target in the case of a symmetric flyer-plate impact (associated with a thinner projectile): (a) propagation of two diverging incident shocks; (b) incident shock reflection from the unrestrained surfaces and the propagation of the resulting decompression shocks within the target; (c) after intersection of the two decompression shocks, the target material bounded by these shocks is in the state of tension; (d) assuming that the tensile-stress level is high enough, spallation takes place (after a short incubation period)

It should be noted that material state 5 has not been mentioned in the foregoing analysis. The reason for this is that this material state is of interest only in the case when spall-fracture does not occur. There are two general scenarios associated with the absence of spall-fracture: (a) The level of tension associated with the material state 4 is not high enough relative to the materials' fracture strength; and (b) the tensile-stress level in question is sufficiently high but the spallation incubation time is too long so that the tensile stress at the candidate spall plane is relieved before spall-fracture can take place. This tension-relief (also referred to as the recompression) process is associated with the reflection of the right-propagating decompression shock from the target back face. This reflection produces a recompression shock which decreases the target back face particle-velocity to zero while leaving the axial stress at the zero value. The zero particle-velocity and zero axial stress material state associated with the passage of the (left-propagating) recompression shock are referred to as state 5.

3.3 Detection of Spall-Fracture

Under extreme conditions, spall-fracture results in the formation of a thin sheet-like fragment from the target back face. Under less severe conditions, spallation produces planes of discrete or connected flaws/defects which could be identified and characterized using conventional destructive and non-destructive metallurgical material-characterization techniques. In this section, it is demonstrated how monitoring of the target back face particle-velocity history can be used to detect the onset of spall-fracture in the target subjected to a symmetric flyer-plate impact.

The no-spallation case is analyzed in Fig. 4(a) to (d). In Fig. 4(a), a conventional post-impact time, t vs. the Lagrangian (uniaxial) spatial coordinate, X, plot is depicted. It should be noted that material state 5 as well as several additional material states are denoted in this figure. Of particular interest is material state 8. This state is produced in the target back face region by the reflection of the recompression shock (generated at the projectile/target interface). This reflection, at the target back face, increases the particle-velocity from its zero value associated with material state 5 to a $\dot{x}_P$ value while leaving the stress at its zero value. Using a simple geometrical analysis and assuming a constant Lagrangian shock speed, U_s, the time period over which the target back face resides in material state 5 can be computed as: $t_5 = 2(L_p - L_T)/U_s$.

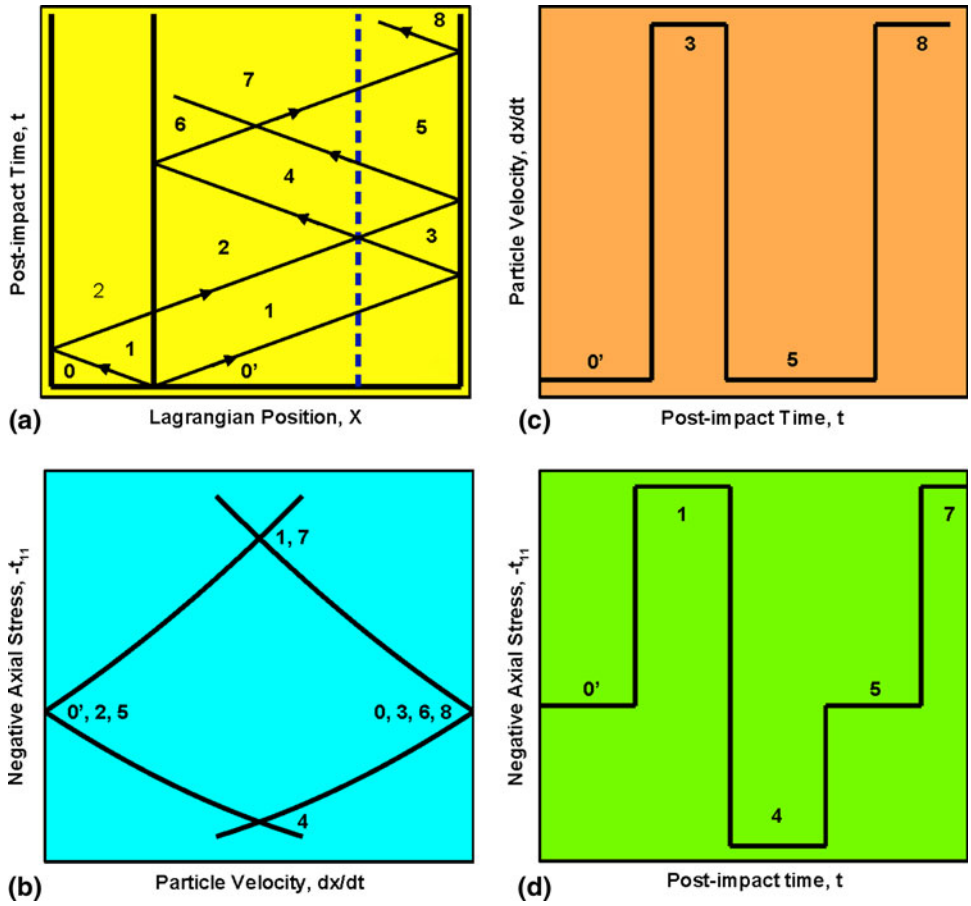

Fig. 4 Key plots describing the outcome of a symmetric flyer-plate experiment in the absence of spall-fracture: (a) t vs. X plot; (b) various $-t_{11}$ vs. $\dot{x}$ Hugoniots and the associated states; (c) particle-velocity temporal evolution at the target back face; and (d) negative axial stress temporal evolution at the candidate spall plane

In Fig. 4(b), a set of $-t_{11}$ vs. $\dot{x}$ Hugoniot curves and the associated material states are presented. These curves are obtained by carrying out a simple shock-jump equation-based analysis of the symmetric flyer-plate impact problem. The results displayed in Fig. 4(b) clearly show that the material state 4 is associated with tensile stresses.

The corresponding history of the target back face particle-velocity along with the associated material states is depicted in Fig. 4(c). For future comparison with the spallation case, one should take note of the total time the target back face material resides in state 5. Furthermore (axial) stress history at the candidate spall plane is shown in Fig. 4(d). It is seen that, as mentioned earlier, the tensile state of the material associated with the material state 4 is relaxed to the zero-stress level as the material changes to state 5.

The spallation case is analyzed in Fig. 5(a) to (d). The t vs. X plot corresponding to this case is shown in Fig. 5(a). It is assumed that there is a finite incubation period for the onset of spallation. The target material at the candidate spall plane resides in the material state 4 during the incubation period. Spall-fracture at the candidate spall plane produces two diverging recompression shocks. The right-propagating recompression shock ultimately reflects from the target back face producing ($\dot{x} = \dot{x}_P$ and $-t_{11} = 0$) material state 9. In the no-spallation case above, it was shown that the maximum time period over which the target back face is in the material state 5 is $t_5 = 2(L_p - L_T)/U_s$.

In Fig. 5(b), the associated $-t_{11}$ vs. $\dot{x}$ Hugoniot curves and the corresponding material states are depicted. These curves were obtained using a procedure analogous to the one employed in the no-spallation case.

In Fig. 5(c), the target back face particle-velocity history is shown in the case when spallation takes place after a brief incubation period. A comparison of the results displayed in Fig. 4(c) and 5(c) reveals that spallation lowers the time period over which the target back face is associated with material state 5. Thus, monitoring the target back face particle-velocity and determining the time period over which the target back face is in the zero particle-velocity material state 5 enables detection of the onset as well as the minimum projectile velocity at which spall-fracture occurs. By carrying out a simple analysis of the flyer-plate problem which involves a combined use of the shock-jump equations and a material-Hugoniot relation, enables determination of the associated tensile-stress level at which the spall-fracture occurs. This could be understood by analyzing Fig. 5(b). The tensile-stress level associated with material state 4 under the minimum projectile initial velocity at which spallation occurs defines the material spall-strength. When the spallation process is detected then the total time the target back face material resides in the material state 5 is equal to the incubation period. It should be noted, however, that the material fracture strength is considered to be a deterministic quantity in this case and that spallation will occur at the spall candidate plane since this plane will first reach the condition for the onset of spallation.

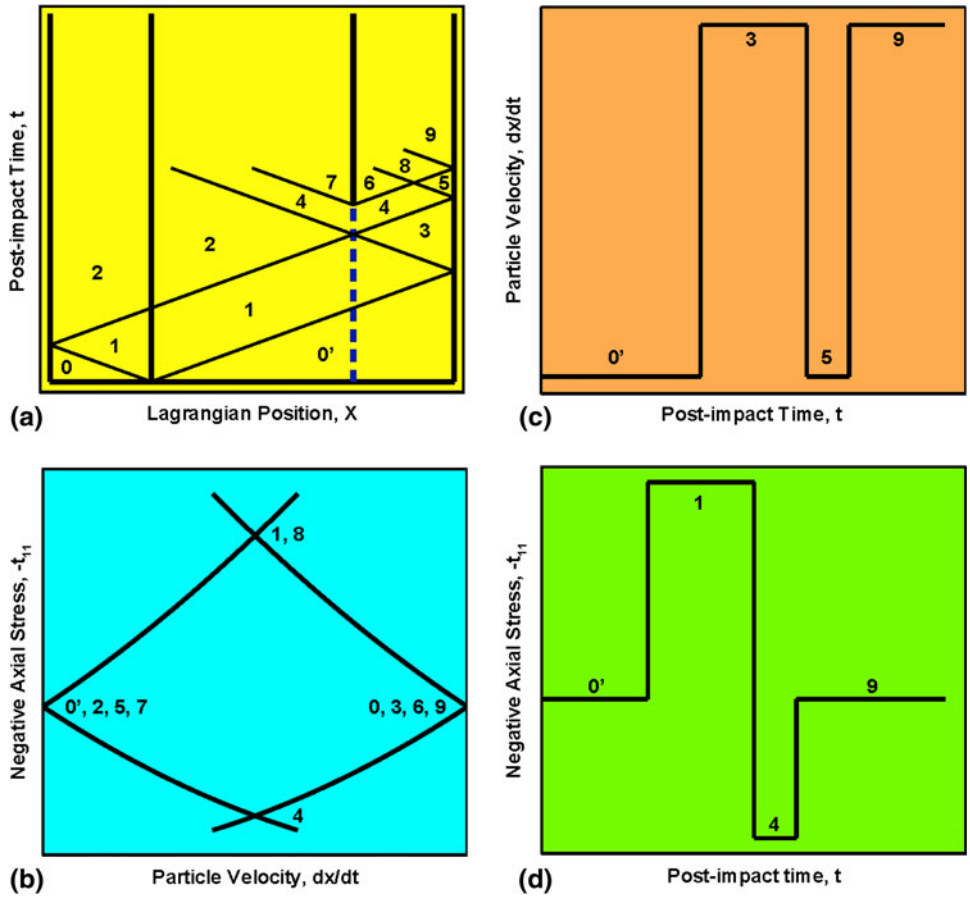

Fig. 5 Key plots describing the outcome of a symmetric flyer-plate experiment in the presence of spall-fracture: (a) t vs. X plot; (b) various $-t_{11}$ vs. $\dot{x}$ Hugoniots and the associated states; (c) particle-velocity temporal evolution at the target back face; and (d) negative axial stress temporal evolution at the candidate spall plane

The stress history at the candidate spall plane is depicted in Fig. 5(d). It is seen that tensile stress ceases at the candidate spall plane at the moment of spallation when the material acquires the (zero-stress) state 9.

It should also be noted that all the quantitative analyses carried out in this study were done under the assumption that the material-Hugoniot relation can be defined by a linear relationship between the Lagrangian shock speed and the particle-velocity as $U_s = C_0 + s\dot{x}$, where C_0 and s are material-specific constants. Under these circumstances a material is fully defined by its parameters C_0, s, ρ_R (reference mass-density) and $t_{11,Spall}$ (a tensile/spall-fracture strength).

4. Spallation Due to Colliding Simple Decompression Waves

In the previous section, for simplicity, decompression smooth waves were approximated by the corresponding decompression shocks. In this section, the decompression waves are more properly treated as centered simple continuous/smooth waves. The term "centered" is used to denote the fact that all the characteristics of the wave emanate from the same (t vs. X) point, the point associated with the arrival of the corresponding incident shock to the projectile/target back face. The term "simple," on the other hand, is used to denote the fact that the leading wavelet/characteristic of the decompression wave advances into a spatially uniform as-shocked material state. It should be recalled that the passage of a centered simple wave through a material point causes the associated material state to change along an isentrope. As mentioned earlier, a weak-shock approximation is used in this study which allows the material isentropes to be replaced with the corresponding material-Hugoniot relations, and vice versa.

4.1 No-Spallation Case

An example of the t vs. X plot obtained in this portion of the study is displayed in Fig. 6. This figure is obtained for the case of a 5 mm thick uranium projectile impacting a 10 mm thick uranium target at an initial velocity of 500 m/s. The four uranium material parameters are defined as: $C_0 = 2487$ m/s, $s = 2.2$, $\rho_R = 18950$ kg/m^3, and $t_{11,Spall} = 2.4$ GPa.

Examination of Fig. 6 shows that upon the reflection of the incident shocks from their respective material unrestrained surfaces, two approaching centered simple decompression waves are formed. The wave front of these waves continuously expands as they propagate through the material. The two waves ultimately intersect forming an interaction region (outlined by four vertices denoted as A, B, C, and D). Within the interaction region, the initially straight decompression-wave characteristics bend upward (as a result of the interaction between the two "finite-amplitude" non-linear waves). Once the two waves

have passed through the interaction region, their characteristics become straight again (and continue to diverge).

As in the case of intersection of two decompression shocks, the interaction of two centered simple decompression waves also creates a material region subjected to tensile stresses. However, stress distribution within this region is highly non-uniform both spatially and temporally. Figure 7 shows stress histories at the spatial location associated with vertices *A*, *C*, and *D*. Examination of the three curves displayed in Fig. 7 shows a number of discontinuities. These discontinuities are associated with abrupt changes in the material state resulting from the passage of the constant *X* material points through different non-interacting and interacting regions of the two decompression waves. The results displayed in Fig. 7 show that the maximum tensile-stress level attained ca. 9.1 GPa greatly exceeds the tensile strength of uranium ($-t_{11,\mathrm{Spall}} = 2.4$ GPa). This condition would certainly lead to spall-fracture which would modify both the *t* vs. *X* (Fig. 6) and the $-t_{11}$ vs. *t* (Fig. 7) plots. These changes are analyzed in the next section.

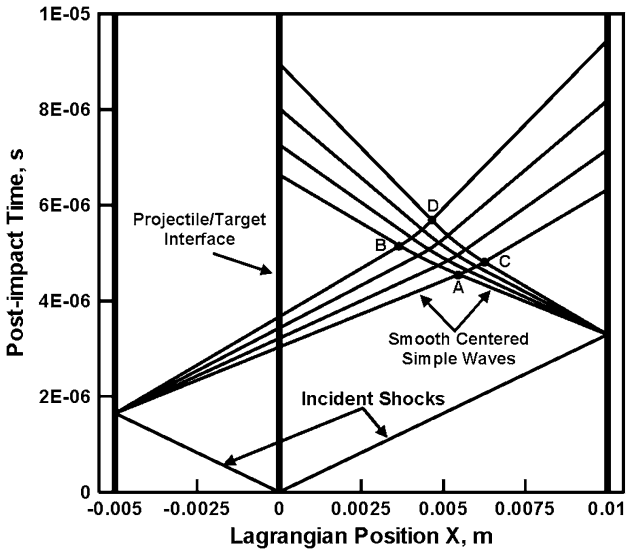

Fig. 6 *t* vs. *X* plot for the case of a uranium symmetric flyer-plate impact in the absence of spallation. The projectile thickness is 5 mm, its initial velocity: 500 m/s, while the target thickness is 10 mm. The intersection of the two centered simple decompression waves produces an interaction region (denoted by vertices *A*, *B*, *C*, and *D*). The *ABC* portion of this region is subjected to compression while the *BCD* portion is subjected to tension

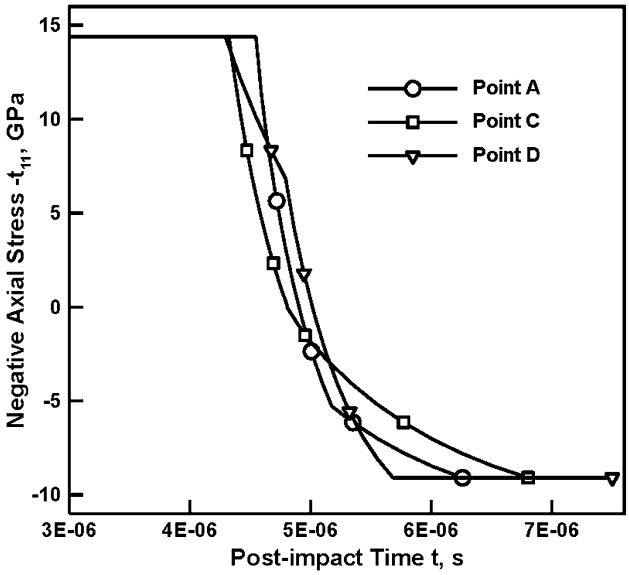

Fig. 7 Temporal evolution of the negative axial stresses at the Lagrangian location of the vertices *A*, *C*, and *D* shown in Fig. 6

4.2 Spallation Case

4.2.1 Simplifying Assumptions. To simplify the analysis, the spall-fracture process resulting from the interaction of two decompression waves is carried out in the limit of zero incubation period. Thus, spallation will occur at the material point at which the tensile stress first becomes equal to the material spall-strength. Examination of the no-spallation results presented in Fig. 6 and 7 revealed that tensile stresses of the largest magnitude are associated with the CD boundary of the decompression-wave interaction region. It should be noted that this boundary coincides with the trailing wavelet/characteristic of the left-propagating centered simple decompression wave.

4.2.2 Spallation. Detailed examination of the stress distribution along the CD boundary shows that the tensile stress becomes equal in magnitude with the material fracture/spall-strength at the spatial location $X = 5.91$ mm ($X = 0$ is placed at the projectile/target interface) and at a post-impact time $t = 4.95$ μs. Accordingly, spall-fracture occurs at this spatial location and at this post-impact time. Due to the formation of two unrestrained surfaces, two diverging recompression shocks are formed. The material swept by each of these shocks is set into zero-stress state. The Hugoniots associated with the two recompression shocks are centered at or originate from the (pre-spallation) "isentropic" material state associated with the material location at which spall-fracture occurred.

The *t* vs. *X* plot for the spallation case is given in Fig. 8. To understand changes in this plot brought about by the spall-fracture process, a comparison should be made between Fig. 6 and 8.

4.2.3 Trajectory of the Right-Propagating Recompression Shock. The next task is to determine the trajectory of the right-propagating recompression shock. The interest is focused on this shock since its arrival to the target back face will drastically alter the back face particle-velocity history. As in section 3, it will be shown that monitoring the history of target back face particle-velocity can be used to both detect the onset of spallation and to quantify the spall-fracture material parameters.

The trajectory (t_s vs. X_s) of the recompression shock in question is described parametrically as:

$$X = X_s(\Delta) \quad \text{and} \quad t = t_s(\Delta) \qquad \text{(Eq 1)}$$

where $\Delta = 1 - \rho_R/\rho$ is the Lagrangian compression and ρ the current mass-density. The linear characteristics of the right-propagating centered simple decompression wave after passage through the interaction region are defined as:

$$X - X_{CD}(\Delta) = C_L(\Delta)[t - t_{CD}(\Delta)] \qquad \text{(Eq 2)}$$

where $C_L(\Delta)$ is the compression-dependent Lagrangian wave speed, while $X_{CD}(\Delta)$ and $t_{CD}(\Delta)$ define the point of emergence of a given Δ characteristic from the interaction region. It should be noted that $X_{CD}(\Delta)$ and $t_{CD}(\Delta)$ which define

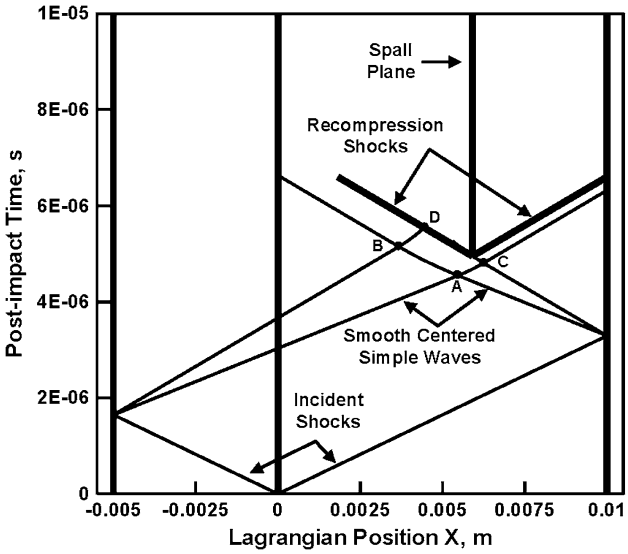

Fig. 8 t vs. X plot for the case of a uranium symmetric flyer-plate impact in the presence of spallation. The projectile thickness is 5 mm, its initial velocity: 500 m/s, while the target thickness is 10 mm. The intersection of the two centered simple decompression waves produces an interaction region (denoted by vertices A, B, C, and D). Spallation and the formation of two diverging recompression shocks takes place at $X = 5.91$ mm and $t = 4.95$ μs

parametrically the CD boundary of the interaction region are known functions which were obtained in the numerical procedure carried out in the no-spallation case.

Along the trajectory of the right-propagating recompression shock, the following functional relationships hold:

$$\mathrm{d}X_\mathrm{s} = U_\mathrm{s}(\Delta)\,\mathrm{d}t_\mathrm{s} \tag{Eq 3}$$

and

$$\frac{\mathrm{d}X_\mathrm{s}(\Delta)}{\mathrm{d}\Delta} = U_\mathrm{s}(\Delta)\frac{\mathrm{d}t_\mathrm{s}(\Delta)}{\mathrm{d}\Delta} \tag{Eq 4}$$

It should be noted that the shock speed is taken to be compression dependent since the right-propagating shock will intersect (and acquire the Δ value of) the characteristics of the right-propagating centered simple decompression wave.

The mass and linear-momentum-based Lagrangian shock-jump equations can be defined as:

$$U_\mathrm{s}\|\Delta\| = \|\dot{x}\| \tag{Eq 5}$$

$$\rho_\mathrm{R} U_\mathrm{s}\|\dot{x}\| = \|-t_{11}\| \tag{Eq 6}$$

where $\|\ldots\|$ denotes a shock-induced jump in a given material state variable. Combining Eq 5 and 6 yields:

$$U_\mathrm{s}^2 = \frac{\|-t_{11}\|}{\rho_\mathrm{R}\|\Delta\|} \tag{Eq 7}$$

Since the material state behind the right-propagating recompression shock is associated with $-t_{11} = 0$, $\Delta = \Delta^{(2)}$ and the associated Hugoniot is approximated with the corresponding $-t_{11}^{(\eta)}$ isentrope, Eq 7 becomes:

$$U_\mathrm{s}^2 = \frac{-t_{11}^{(\eta)}(\Delta)}{\rho_\mathrm{R}(\Delta^{(2)} - \Delta)} \tag{Eq 8}$$

Under the condition that the "Gruneisen Gamma" parameter $\gamma(v) = \frac{\gamma_\mathrm{R}}{v_\mathrm{R}}v$, where v is the specific volume, the $-t_{11}^{(\eta)}$ isentrope can be defined as:

$$-t_{11}^{(\eta)}(\Delta) = \chi_\mathrm{c}(\Delta)\left\{t_{11}^{+} + \int_{\Delta^+}^{\Delta}\frac{\kappa_\mathrm{c}(\Delta')}{\chi_\mathrm{c}(\Delta')}\,\mathrm{d}\Delta'\right\} \tag{Eq 9}$$

where

$$\chi_\mathrm{c}(\Delta) = \exp\left[\gamma_\mathrm{R}(\Delta - \Delta^+)\right] \tag{Eq 10}$$

$$\kappa_\mathrm{c}(\Delta) = \left(1 - \frac{\gamma_\mathrm{R}}{2}\Delta\right)\frac{\mathrm{d}t_{11}^{(H)}(\Delta)}{\mathrm{d}\Delta} - \frac{\gamma_\mathrm{R}}{2}t_{11}^{(H)}(\Delta) \tag{Eq 11}$$

$$-t_{11}^{(H)}(\Delta) = \frac{\rho_\mathrm{R}C_\mathrm{B}^2\Delta}{(1 - S\Delta)^2} \tag{Eq 12}$$

and

$$C_\mathrm{L}(\Delta) = \left\{\frac{1}{\rho_\mathrm{R}}\left[p^{(\eta)}(\Delta) + \kappa_\mathrm{c}(\Delta)\right]\right\}^{1/2} \tag{Eq 13}$$

Furthermore, the following equations can be readily derived:

$$\frac{\mathrm{d}C_\mathrm{L}(\Delta)}{\mathrm{d}\Delta} = \frac{1}{2\rho_\mathrm{R}C_\mathrm{L}(\Delta)}\left\{\gamma_\mathrm{R}^2 p^{(\eta)}(\Delta) + \gamma_\mathrm{R}\kappa_\mathrm{c}(\Delta) + \frac{\mathrm{d}\kappa_\mathrm{c}(\Delta)}{\mathrm{d}\Delta}\right\} \tag{Eq 14}$$

$$\frac{\mathrm{d}\kappa_\mathrm{c}(\Delta)}{\mathrm{d}\Delta} = \frac{\rho_\mathrm{R}C_\mathrm{B}^2}{(1 - S\Delta)^4}\left[3S + (S - \gamma_\mathrm{R})(1 + 2S\Delta)\right] \tag{Eq 15}$$

According to Eq 2, the intersection of the right-propagating recompression shock with the characteristics of the right-propagating decompression waves is defined as:

$$X_\mathrm{s}(\Delta) - X_\mathrm{CD}(\Delta) = C_\mathrm{L}(\Delta)[t_\mathrm{s}(\Delta) - t_\mathrm{CD}(\Delta)] \tag{Eq 16}$$

Differentiation of Eq 16 with respect to Δ yields:

$$\frac{\mathrm{d}X_\mathrm{s}(\Delta)}{\mathrm{d}\Delta} - \frac{\mathrm{d}X_\mathrm{CD}(\Delta)}{\mathrm{d}\Delta} = [t_\mathrm{s}(\Delta) - t_\mathrm{CD}(\Delta)]\frac{\mathrm{d}C_\mathrm{L}(\Delta)}{\mathrm{d}\Delta} + C_\mathrm{L}(\Delta)\left[\frac{\mathrm{d}t_\mathrm{s}(\Delta)}{\mathrm{d}\Delta} - \frac{\mathrm{d}t_\mathrm{CD}(\Delta)}{\mathrm{d}\Delta}\right] \tag{Eq 17}$$

Substitution of Eq 4 into 17 gives:

$$\frac{\mathrm{d}t_\mathrm{s}(\Delta)}{\mathrm{d}\Delta} + \phi(\Delta)t_\mathrm{s}(\Delta) = \Psi(\Delta) \tag{Eq 18}$$

where

$$\phi(\Delta) = \frac{1}{C_\mathrm{L}(\Delta) - U_\mathrm{s}(\Delta)}\frac{\mathrm{d}C_\mathrm{L}(\Delta)}{\mathrm{d}\Delta} \tag{Eq 19}$$

$$\Psi(\Delta) = \frac{\frac{\mathrm{d}X_\mathrm{CD}(\Delta)}{\mathrm{d}\Delta} - C_\mathrm{L}(\Delta)\frac{\mathrm{d}t_\mathrm{CD}(\Delta)}{\mathrm{d}\Delta} - t_\mathrm{CD}(\Delta)\frac{\mathrm{d}C_\mathrm{L}(\Delta)}{\mathrm{d}\Delta}}{U_\mathrm{s}(\Delta) - C_\mathrm{L}(\Delta)} \tag{Eq 20}$$

where Eq 4 was used to eliminate $\frac{\mathrm{d}X_\mathrm{s}(\Delta)}{\mathrm{d}\Delta}$.

Equation 18 is a standard linear first-order ordinary differential equation which can be reduced to a quadrature (an integral disguised as an ordinary differential equation). Hence, Eq 18 can be readily integrated to get $t_\mathrm{s}(\Delta)$. Then $X_\mathrm{s}(\Delta)$ can be obtained from Eq 16 to complete the definition of the trajectory of the right-propagating recompression shock.

4.2.4 Particle-Velocity History of the Target Back Face. Particle-velocity history at the target back face in the presence of spallation is shown in Fig. 9 (using a solid curve). For comparison, the particle-velocity history at the target back face in the absence of spallation is also shown in the same figure (as a dashed curve). A comparison of the two curves shows that arrival of the right-propagating recompression shock to the target back face gives rise to an abrupt change in the particle-velocity at the target back face to a value nearly equal to the projectile initial velocity. This phenomenon is commonly referred to as the "pull-back signal." As in the decompression-shock case, determination of the post-impact time at which the pullback signal is detected can be used to quantify the materials' spall-strength. This is demonstrated in Fig. 10 in which the relationship between the material spall-strength and the post-impact time at which the pull-back signal arrives at the target back face is plotted for the case of uranium symmetric flyer-plate impact (the projectile thickness is 5 mm, its initial velocity 500 m/s, while the target thickness is 10 mm). This plot which was generated using the numerical procedure described earlier in this section enables one to determine the material spall-strength using the measured values of the pull-back signal arrival time to the target back face.

5. Spallation-Strength-Based Material Selection

In this section, an attempt is made to establish a criterion for the selection of materials for the use in the protective structures in which the absence of spall-fracture is an important functional requirement. A separate consideration will be given to the cases where spallation is the result of intersection of two decompression shocks and the interaction of two decompression smooth waves.

5.1 Decompression Shock-Based Analysis

Examination of Fig. 5(b) shows that in the symmetric flyer-plate case, the material state 4 experiencing the maximum tension, is associated with a particle-velocity equal to one half of the projectile initial velocity. Based on this finding, the material-selection criterion derived here is defined by imposing the requirement that the material should be able to sustain the highest possible projectile initial velocity without spalling (Ref 9). Material selection is then carried out using the following procedure:

(a) First, it is recognized that the $-t_{11}$ vs. $\dot{x}$ Hugoniot relation derived within the Lagrangian framework is:

$$-t_{11} = \rho_R U_s \dot{x} = \rho_R (C_0 + S\dot{x})\dot{x} \qquad \text{(Eq 21)}$$

If the $-t_{11}$ vs. $\dot{x}$ Hugoniot is drawn to pass through $-t_{11} = 0$, $\dot{x} = 0$ point, material state 4 in this case, corresponds to $\dot{x} = -\dot{x}_P/2$. If at the onset of spall-fracture, the projectile critical velocity denoted as $\dot{x}_{\text{ProjCrit}}$, then the corresponding material state 4 is associated with $t_{11} = t_{11,\text{Spall}}$ and $\dot{x} = \frac{\dot{x}_{\text{ProjCrit}}}{2}$;

(b) After substitution of these material state conditions into Eq 21 one obtains:

$$\rho_R \left(C_0 - S\frac{\dot{x}_{\text{ProjCrit}}}{2}\right)\left(-\frac{\dot{x}_{\text{ProjCrit}}}{2}\right) = -t_{11,\text{Spall}} \qquad \text{(Eq 22)}$$

or

$$\frac{\rho_R S \dot{x}_{\text{ProjCrit}}^2}{4} - \frac{\rho_R C_0 \dot{x}_{\text{ProjCrit}}}{2} + t_{11,\text{Spall}} = 0 \qquad \text{(Eq 23)}$$

The solution of Eq 23 yields

$$\dot{x}_{\text{ProjCrit}} = \frac{C_0}{S} - \sqrt{\left(\frac{C_0}{S}\right)^2 - \frac{4t_{11,\text{Spall}}}{\rho_R S}} \qquad \text{(Eq 24)}$$

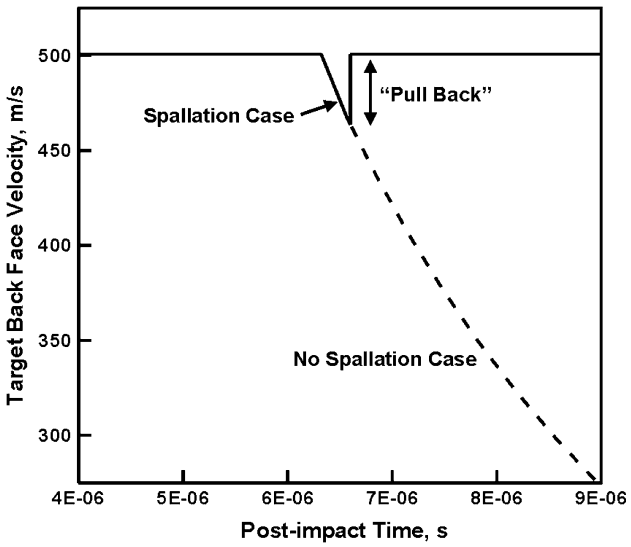

Fig. 9 Temporal evolution of the particle-velocity at the target back face in the absence (dashed line) and in the presence (solid line) of spall-fracture for the case of uranium symmetric flyer-plate impact. The projectile thickness is 5 mm, its initial velocity 500 m/s, while the target thickness is 10 mm

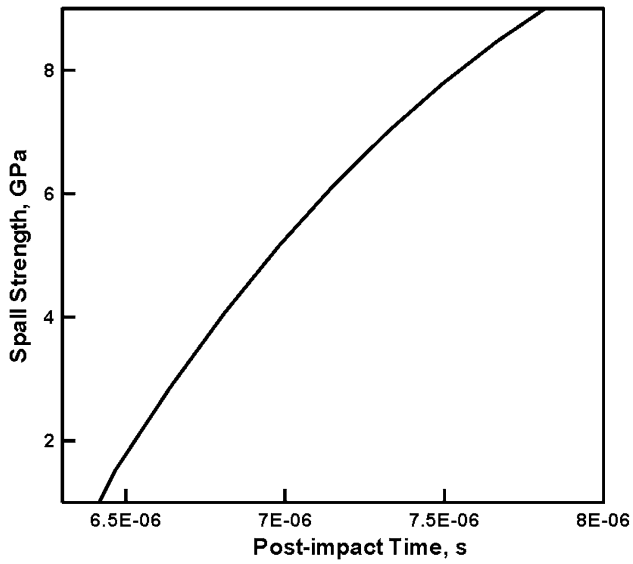

Fig. 10 Relationship between the material spall-strength and the post-impact time at which the pull-back signal arrives at the target back face for the case of uranium symmetric flyer-plate impact. The projectile thickness is 5 mm, its initial velocity 500 m/s, while the target thickness is 10 mm

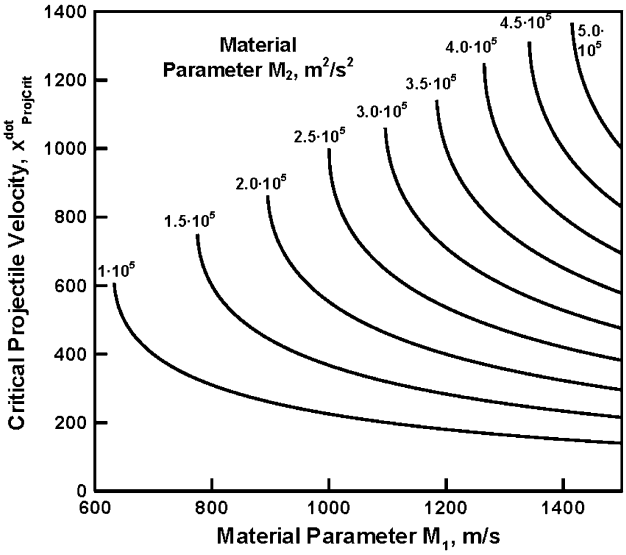

Fig. 11 Spall-strength-based material-selection chart. Please see text for the explanation of material indices M_1 and M_2

The four material parameters C_0, S, ρ_R, and $t_{11,\text{Spall}}$ can be grouped into two spallation-strength-based material-selection parameters:

$$M_1 = \frac{C_0}{S}; \quad M_2 = \frac{t_{11,\text{Spall}}}{\rho_R S} \qquad \text{(Eq 25)}$$

Figure 11 shows a series of $\dot{x}_{\text{ProjCrit}}$ vs. M_1 curves each associated with a different constant level of the material parameter M_2. The way this plot is used in the material-selection process is as follows:

(a) material parameters M_1 and M_2 are computed first;
(b) if the iso-M_2 curve in question is not available in Fig. 11, it should be approximated using the available iso-M_2 curves and a simple interpolation scheme; and
(c) the (M_1, M_2) point should be placed onto the newly constructed iso-M_2 curve and the associated $\dot{x}_{\text{ProjCrit}}$ read from the Fig. 11 ordinate. Alternatively, Eq 24 can be evaluated for the material under consideration. Clearly, the higher the value of $\dot{x}_{\text{ProjCrit}}$ the more suitable is the material for use in the (symmetric flyer-plate) applications in which low probability of spall-fracture is required.

When the aforementioned procedure(s) is applied to four standard metallic materials the following ranking and the projectile maximum initial velocities are obtained: 1 = Aluminum-2024, 137 m/s; 2 = Steel-1006, 118 m/s; 3-commercially pure Uranium, 107 m/s; and 4-commercially pure Copper, 80 m/s.

5.2 Centered Simple Decompression-Wave-Based Analysis

In this case, material selection is carried out using the same functional requirement, i.e., the material must be able to survive a maximum projectile velocity before spall-fracture can take place. However, due to the complexity of the analysis, there is no easy way for defining the appropriate material-selection parameters or to cast this requirement in a single functional form (like Eq 24). Nevertheless, the maximum projectile velocity before spallation can be still calculated using the numerical procedure presented in section 4. As explained earlier, stress becomes increasingly tensile along the CD boundary of the interaction region, Fig. 6, so that the maximum tensile stress (in the absence of spallation) is associated with vertex D. Based on this observation, the functional requirement in question is restated as a requirement that the target must be able to endure an impact with a maximum projectile velocity without having the stress level at vertex D reach the spall-strength. One can then run a series of numerical calculations at different projectile initial velocities to define the projectile critical velocity more accurately.

When this procedure is applied to the four candidate materials the same ranking as that in the decompression-shock case was obtained. That is: 1 = Aluminum-2024; 2 = Steel-1006; 3-commercially pure Uranium; and 4-commercially pure Copper.

The above finding suggests that the simpler decompression-shock-based material-selection procedure is adequate (at least in the weak-shock regime, assumed here). It should be noted that due to the weak-shock approximation used, tensile-stress levels associated with the same projectile initial velocity are quite similar (within a fraction of a percent) in the decompression-shock and the decompression-wave cases.

6. Summary and Conclusions

Based on the material presented in this study, the following main summary remarks and conclusions can be drawn:

1. The phenomenon of spall-fracture in target structures impacted with a high-velocity projectile is analyzed within the context of shock and finite-amplitude wave physics;
2. Spallation is shown to result from the interaction of decompression waves.

When these waves are treated as decompression shocks, it is shown that spall-strength-based material selection can be carried out using a relatively simple procedure involving two material-selection parameters.

3. On the other hand, when these waves are treated as centered simple finite-amplitude waves, the material selection could be still carried out but requires the use of a more elaborate numerical procedure. Material-selection parameters could not be readily derived in this case.
4. Both approaches, however, yield consistent results relative to the material ranking suggesting that the simpler decompression-shock-based analysis of spall-fracture is appropriate for use in spall-strength-based material-selection process.

Acknowledgments

The material presented in this article is based on study supported by the Office of Naval Research (ONR) research contract entitled "Elastomeric Polymer-By-Design to Protect the Warfighter Against Traumatic Brain Injury by Diverting the Blast Induced Shock Waves from the Head", Contract Number 4036-CU-ONR-1125 as funded through the Pennsylvania State University. The authors are indebted to Dr. Roshdy Barsoum of ONR for continuing support and interest in the present work. The authors would also like to thank Dr. Lee Davison whose

book "Fundamentals of Shock Wave Propagation in Solids" and specifically Chapter 12: Spall-Fracture, provided the motivation and the necessary shock-physics background used in this study.

References

1. M. Grujicic, B. Pandurangan, D.C. Angstadt, K.L. Koudela, and B.A. Cheeseman, Ballistic-Performance Optimization of a Hybrid Carbon-Nanotube/E-glass Reinforced Poly-Vinyl-Ester-Epoxy-Matrix Composite Armor, *J. Mater. Sci.*, 2007, **42**, p 5347–5359
2. L. Davison, *Fundamentals of Shock Wave Propagation in Solids*, Springer, Berlin, Heidelberg, Germany, 2008
3. A. Tarabay, L. Seaman, D.R. Curran, G.I. Kanel, S.V. Razorenov, and A.V. Utkin, *Spall Fracture*, Springer, New York, 2003
4. L. Davison, D.E. Grady, and M. Shahinpoor, Ed., *High-Pressure Shock Compression of Solids II*, Springer, New York, 1996
5. D.E. Grady, *Fragmentation of Rings and Shells: The Legacy of N.F. Mott*, Springer, Heidelberg, 2006
6. G.I. Kanel, S.V. Razorenov, and V.E. Fortov, *Shock-Wave Phenomena and the Properties of Condensed Matter*, Springer, New York, 2004
7. M.A. Meyers and C.T. Aimone, Dynamic Fracture (Spalling) of Metals, *Prog. Mater. Sci.*, 1983, **28**, p 1–96
8. J. S. Rinehart and J. Pearson, *Behavior of Metals under Impulsive Loads*, American Society for Metals, Cleveland (1954). Reprinted by Dover Publications, New York (1965)
9. M. Grujicic, B. Pandurangan, W. C. Bell, and S. Bagheri, Shock-Wave Attenuation and Energy-Dissipation Potential of Granular Materials, *J. Mater. Eng. Perform*. doi:10.1007/s11665-011-9954-8, 2010